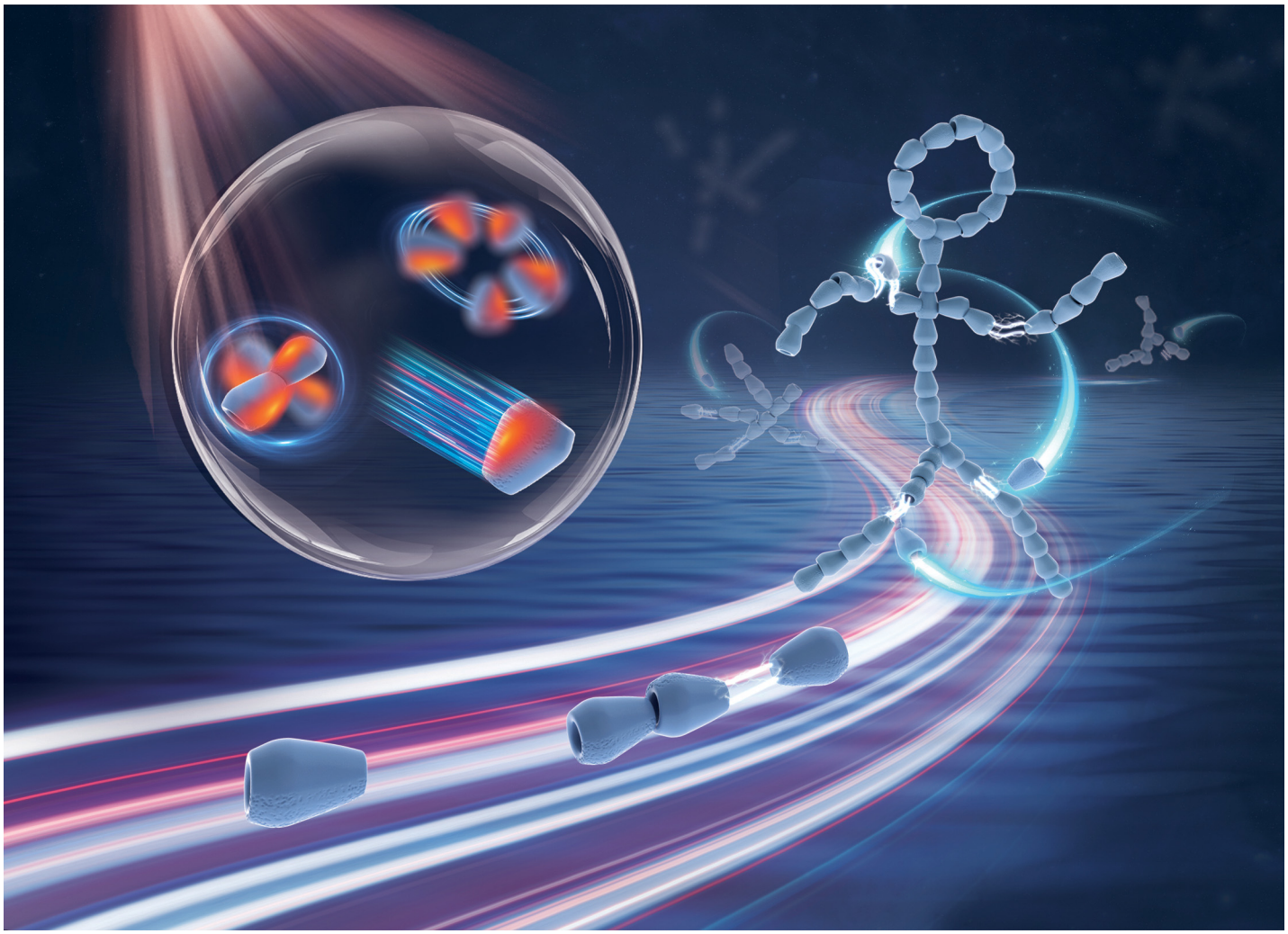

Showcasing research from Professor Pingan Zhu's laboratory at the Department of Mechanical Engineering, City University of Hong Kong, Hong Kong, China.

Programmable assemblies of photothermal anisotropic micromotors for multimodal motion

Highly controllable, programmable, and customizable self-assembly of photothermal Marangoni micromotors enables versatile multimodal motion, including translation, revolution, rotation, and their combinations.

As featured in:

See Pingan Zhu *et al.*, *Mater. Horiz.*, 2025, **12**, 1168.

ROYAL SOCIETY OF CHEMISTRY

rsc.li/materials-horizons

Registered charity number: 207890

Materials Horizons

ROYAL SOCIETY OF CHEMISTRY

COMMUNICATION

View Article Online
View Journal | View Issue

Cite this: *Mater. Horiz.*, 2025, **12**, 1168

Received 27th September 2024,
Accepted 2nd January 2025

DOI: 10.1039/d4mh01346h

rsc.li/materials-horizons

Programmable assemblies of photothermal anisotropic micromotors for multimodal motion†

Wenchang Zhao, [a] Shiyu Wang, [a] Ying Zhou,[a] Yanhong Li,[a] Shuxian Tang,[a] Yutong Zheng[a] and Pingan Zhu *[ab]

Light-driven micromotors with multiple motion modes offer significantly greater application potential than single-mode micromotors. However, achieving such versatility often requires complex structural designs and precise light focusing on specific micromotor regions, presenting challenges for dynamic operations and microscale precisions. This study introduces programmable assemblies of anisotropic micromotors driven by the photothermal Marangoni effect, produced in bulk *via* microfluidic technology. Under full-area near-infrared (NIR) irradiation, the micromotor exhibits multiple motion modes, including translation and revolution, while micromotor assemblies display additional rotational motion. Self-assembly of these micromotors is highly controllable and programmable, enabling easy customization of assembled structures to achieve desired motion modes. These features are expected to advance the development of various intelligent self-propelling systems, using multimodal individual micromotors as foundational building blocks.

New concepts

The realization of light-driven micromotors with multiple motion modes typically depends on complex structural designs and precise light-focusing strategies, which increases system complexity and cost while posing challenges for precise dynamic operations and microscale tasks. Unlike conventional approaches, this study leverages easy-fabricated anisotropic micromotors under full-area infrared irradiation to achieve multimodal motion. Individual micromotors exhibit translation and revolution, while micromotor assemblies demonstrate additional rotational motion. These micromotors are produced in bulk *via* microfluidic technology without the need for subsequent functionalization. Notably, their self-assembly process is highly controllable and programmable, facilitating the customization of assembled structures to achieve desired motion modes. This system inspires the development of more advanced multi-mode micromotors in the future.

1. Introduction

Micromotors are miniature machines that convert energy into efficient mechanical motion, finding extensive applications in cargo transport,[1,2] environmental remediation,[3,4] sensing,[5] and drug delivery,[6,7] to name a few. Various propulsion mechanisms, including magnetic fields,[8–10] electric controls,[11,12] chemicals,[13,14] and light,[15–17] have been developed to propel micromotors. Light-driven propulsion stands out due to its non-contact operation, extended lifespan, and rapid responsiveness. The photothermal effect converts light into thermal energy, generating local temperature gradients that induce Marangoni flows driven by surface tension variations.[18,19] Unlike surfactant-fueled Marangoni micromotors, which are limited by finite surfactant capacity and cease functioning upon fuel depletion,[20,21] light-driven thermal Marangoni micromotors operate fuel-free, overcoming this critical limitation.[22,23] Moreover, light offers advantages in remote, contactless control with high spatial and temporal precision, enabling fine-tuned manipulation of motion, including on-demand "on" and "off" motions, speed adjustment, and transition between motion modes through variations in wavelength and intensity.[24] The versatility, accessibility, and remote controllability of light-driven thermal Marangoni micromotors make them highly promising for diverse practical applications.

Light-driven micromotors with multiple modes of motion are more desirable than single-function micromotors. For example, linear or curvilinear movements show promise for cargo transport, whereas rotational motion's periodic and continuous nature is advantageous for gear transmission or small-scale mixing.[25] To achieve such versatility, a common strategy involves focusing light on specific regions of the micromotor to generate forces that control its direction of motion.[26,27] However, this approach necessitates dynamically high-precision tracking and focusing of the light,[28–30] presenting challenges for long-

[a] *Department of Mechanical Engineering, City University of Hong Kong, Hong Kong, China. E-mail: pingazhu@cityu.edu.hk*
[b] *Shenzhen Research Institute of City University of Hong Kong, Shenzhen, China*
† Electronic supplementary information (ESI) available. See DOI: https://doi.org/10.1039/d4mh01346h

term and microscale tasks. Full-area illumination is a simpler and more stable strategy, enabling micromotors to perform programmed motion modes without precise light focusing. Nonetheless, full-area illumination typically restricts a micromotor to a single motion mode, such as unidirectional translation[31] or rotation.[32] Achieving diverse motion modes necessitates designing and fabricating micromotors with distinct structural features, which increases system complexity, fabrication challenges, and costs.

An alternative approach involves creating micromotor assemblies[33–35] that mimic natural swarms, such as schools of fish or flocks of birds, which exhibit sophisticated collective behaviors and cooperative functions, including migration and predator avoidance.[36,37] Even when individual micromotors exhibit simple behaviors or functions, their assemblies can display synergistic functionalities surpassing single units.[38,39] However, such assemblies are often random, lacking precise control and organization in their motion behaviors. Previous studies have demonstrated programmable and reversible self-assembly using periodic polymeric micropillar arrays containing magnetic particles.[40] The diversity of assembled structures can be further enhanced by tailoring the anisotropy of the particles. To achieve "customizable" functionalities, it is imperative to develop highly controlled and directed self-assembly processes. Utilizing identical micromotors in self-assembly obviates the need for structural customization of each unit, and appropriate batch manufacturing techniques can significantly reduce the time and complexity of the entire system. Microfluidic technology based on droplet templates can effectively generate a series of droplet molds, which can produce particles with high uniformity and rationally designed shapes and microstructures.[41–43] This makes microfluidic technology a promising platform for the fabrication of versatile micromotors.

This study presents the design and fabrication of programmable micromotor assemblies driven by the photothermal Marangoni effect. The micromotor is constructed from bullet-shaped polydimethylsiloxane (PDMS) microparticles, integrated with unilaterally distributed Fe_3O_4 nanoparticles (Fe_3O_4-NPs), and precisely produced using microfluidic technology. The micromotors' shape anisotropy facilitates the formation of diverse and precise assembly configurations, while their composition anisotropy enables photothermal actuation. The resultant micromotor supports multiple motion modes: under full-area NIR irradiation, individual micromotors exhibit both translation and revolution on the water surface. Additionally, self-assembled micromotor structures, formed through capillary interactions, demonstrate additional rotational motion. Notably, by adjusting the orientation, angle, and relative positions of the micromotors on the water surface, custom assembly patterns can be created to achieve specific motion modes. Furthermore, predefined superstructures can be assembled using either light or magnetic fields. By combining these two fields, the system can achieve more sophisticated motion behaviors, including customizable and arbitrary trajectories. These advanced features hold promise for developing various intelligent self-propelling systems with applications in fields such as information encoding, cargo delivery, and architectural construction.

2. Results

2.1 Photothermal Marangoni micromotor

Fig. 1(a) displays the design of the photothermal Marangoni micromotor, which consists of an anisotropic bullet-shaped PDMS microparticle with Fe_3O_4-NPs distributed asymmetrically on one side. The low density of the composite materials (0.981 kg m^{-3}) and the hydrophobic nature of PDMS enable the micromotor to leverage both capillary and buoyant forces when placed on water. These effects allow the micromotor to easily counteract gravity and float stably on the water surface. Meanwhile, Fe_3O_4-NPs, known for their photothermal conversion properties, absorb NIR light and convert it into heat. As depicted in Fig. 1(a), when the micromotor on the water surface is exposed to full-area NIR irradiation, the Fe_3O_4-NPs absorb the light, generating a temperature gradient across the motor ($T_h > T_l$). This gradient causes an imbalance in surface tension, propelling the micromotor from the low surface tension region (γ_l) to the high surface tension region (γ_h) due to the Marangoni effect, *i.e.*, from the hot region to the cold region. The micromotor's motion is influenced by its orientation on the water surface, resulting in either translation or revolution (Fig. 1(b) and Movie S1, ESI†). As shown in Fig. 1(c), a side view analysis indicates that when the micromotor's axis forms a lying angle (θ) close to 0° with the water surface, it exhibits translational motion. As θ increases, the micromotor tilts, which generates torque and induces revolution.

The micromotors were fabricated using microfluidic technology, as illustrated in Fig. S1a (ESI†).[44] In the co-flow microchannel, the inner phase liquid, consisting of PDMS and Fe_3O_4-NPs, is broken into spherical microdroplets at a frequency of ~2 Hz by the outer phase liquid, a sodium alginate (NaAlg) solution. These microdroplets spontaneously arrange into a uniform droplet array in the NaAlg solution. Microfibers encapsulating the microdroplets are then formed through ion cross-linking as the NaAlg flows into a calcium chloride solution. Due to the parabolic flow velocity profile within the NaAlg microfiber,[45,46] the PDMS/Fe_3O_4 microdroplets experience uneven shear forces, transforming into an anisotropic bullet-like shape with a smaller front and a larger rear end. The distribution of Fe_3O_4-NPs can be controlled by adjusting the PDMS curing process. A long curing time at room temperature allows the nanoparticles to settle to one side, whereas rapid curing at high temperatures (80 °C) results in a uniform nanoparticle distribution. After curing, the anisotropic microparticles are obtained by dissolving the alginate microfibers in an aqueous solution of tetrasodium ethylenediaminetetraacetate (EDTA-4Na).[41]

Optical and scanning electron microscope (SEM) images in Fig. 1(d) provide detailed views of the synthesized bullet-shaped microparticles with side-distributed Fe_3O_4-NPs. The microparticles are uniform in size (Fig. S1b, ESI†), with a length of approximately 700 μm and featuring a hole at the rear end that occupies nearly half of the particle. Notably, the Fe_3O_4-NPs are deposited on one side, resulting in asymmetry in both shape and internal material distribution, positioning these microparticles as multimodal micromotors.

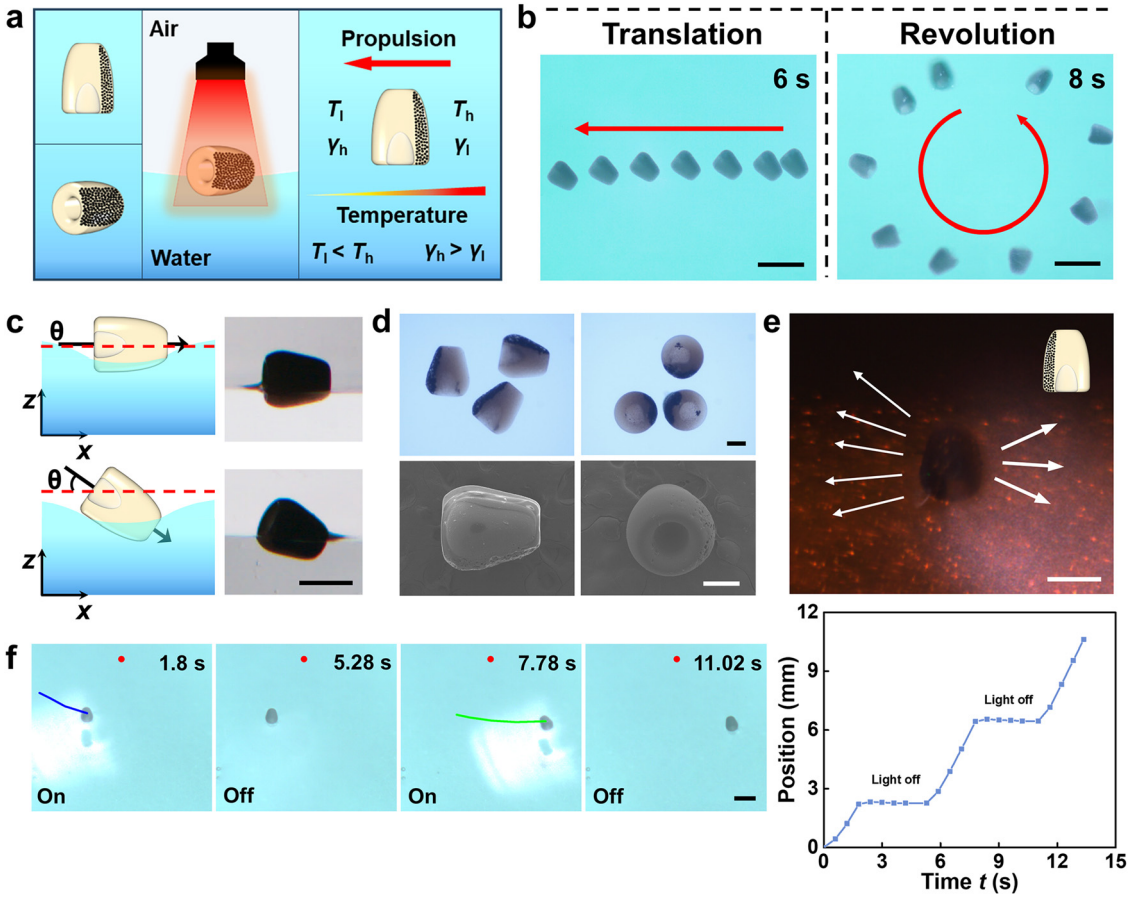

Fig. 1 Photothermal Marangoni micromotor. (a) Schematic of the micromotor under full-area NIR irradiation. The unilateral distribution of Fe_3O_4-NPs generates a temperature gradient, creating a surface tension gradient around the micromotor, driving it toward the colder region. (b) The timelapse of a single micromotor's translation and revolution motion, in which the darker side contains the Fe_3O_4-NPs. (c) Side view of the micromotor with different lying angle θ on the water surface. (d) Optical (top) and scanning electronic microscope (bottom) images of the micromotor. The darker and rough sides indicate the presence of Fe_3O_4-NPs. (e) Distribution of fluorescent tracers around the micromotor under laser irradiation, with white arrows indicating the spontaneous movement of fluorescent particles away from the micromotor. (f) The on-demand motion of micromotors controlled by the switching of NIR illumination. Scale bars, 1 mm in (b), 250 μm in (d), 500 μm in (c) and (e), and 1 mm in (f).

To verify the photothermal Marangoni motion mechanism of the micromotors, we conducted several control experiments. First, we prepared microparticles (1.000 kg m^{-3}) with uniformly distributed Fe_3O_4-NPs and studied their behavior under full-area NIR illumination. As shown in Fig. S1c (ESI†), these microparticles remain almost stationary, confirming the necessity of the temperature gradient created by the asymmetric distribution of Fe_3O_4-NPs for inducing motion. Additionally, when polyvinyl alcohol (PVA, 0.2 wt%) was added to the water to reduce the surface tension effect, the motion was quenched (Fig. S1d, ESI†). These results confirm that the micromotor's movement is driven by the photothermal Marangoni effect. To further explore this mechanism, fluorescent particles were used as tracers to visualize the flow field around the micromotor. As shown in Fig. 1(e) and Movie S2 (ESI†), the surrounding fluorescent particles spontaneously move away from the micromotor, with the effect being more pronounced on the higher-temperature side with Fe_3O_4-NPs. Additionally, the photothermal effect enables precise, on-demand motion control. As shown in Fig. 1(f), repeated on/off cycles of NIR irradiation rapidly activate and deactivate the micromotor's movement, demonstrating a rapid response rate (Movie S3, ESI†). This propulsion behavior offers a distinct advantage, providing enhanced maneuverability compared to other mechanisms, such as solute-fueled Marangoni micromotors.

The temperature gradient across the micromotor determines the surface tension gradient, which drives its motion. Under NIR irradiation, the temperature distribution (Fig. 2(a)) shows that the side of the micromotor containing Fe_3O_4-NPs reaches the highest temperature (T_h), creating a significant temperature difference ($\Delta T = T_h - T_l$) compared to the opposite side (T_l). The typical ΔT ranges from 15 °C to 45 °C and increases with rising power density (Fig. 2(b)). Given the temperature dependence of water surface tension,[47] this ΔT induces a surface tension gradient on the order of several mN m^{-1} across the micromotor, driving its motion. This temperature difference develops rapidly within 1 second, highlighting the highly efficient photothermal effect for fast motion actuation. In a typical experiment, the micromotor's motion speed initially increases with time before stabilizing at a constant value (Fig. 2(c)).

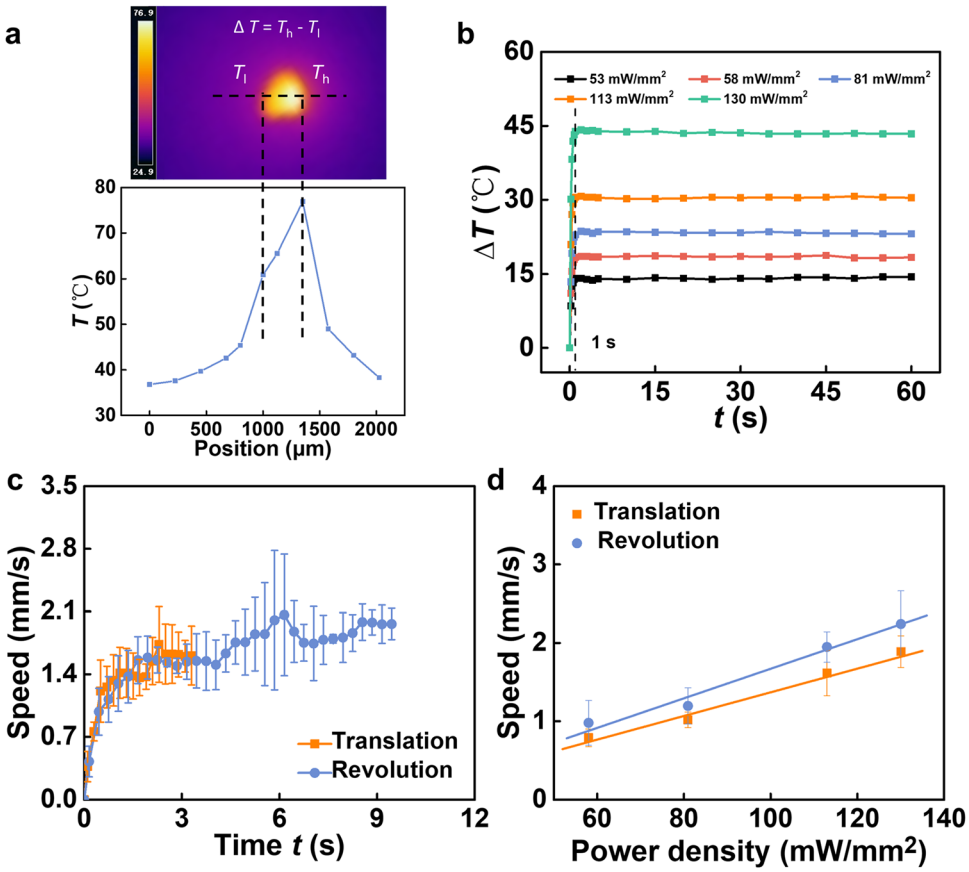

Fig. 2 Photothermal Marangoni effect in micromotors. (a) Temperature field around the micromotor illustrating the thermal gradient, characterized by a temperature difference (ΔT) between the two opposite sides. (b) Relationship between the temperature difference and time under different laser power densities. (c) The plot of the translation and revolution speeds of the micromotor over time under 113 mW mm^{-2} NIR illumination. (d) Speed of translation and revolution motion as a function of laser power density, with solid lines representing linear fitting.

The final constant speed is proportional to the power density (Fig. 2(d)), as higher power density enhances the temperature difference, leading to a stronger surface tension gradient for driving the micromotor's motion.

2.2 Double-micromotor self-assembly

The above description details the motion principle and characteristics of a single micromotor. It is well established that, unlike individual units, groups and assemblies can exhibit complex collective behaviors and cooperative functions in nature. Interestingly, our experiments revealed that multiple micromotors can spontaneously assemble into higher-order structures.

As illustrated in Fig. 3(a), the assembly of micromotors is driven by capillary interactions, where their hydrophobic nature induces the formation of negative menisci when they float on the water's surface. When two micromotors come within a distance smaller than the capillary length (approximately 2–3 mm on the water surface, Note S1, ESI†), their menisci overlap and interact, leading to mutual attraction[48] and subsequent self-assembly into a doublet. The lying angle (θ) of micromotors determines the resulting assembly structures (Movie S4, ESI†). For small θ, the micromotors expose their front ends to the air as much as possible, resulting in a chain-like structure (Fig. 3(a)). For larger θ, the front of micromotors is submerged underwater, leading to a non-chain structure (Fig. 3(b)). Interestingly, micromotors can adjust their orientations during the assembly process. For example, micromotors initially parallel to each other can rotate to form a chain-like structure (Fig. 3(c)). The guiding principle in this orientation adjustment is the tendency to align with the nearest end of another micromotor.

It is worth noting that the self-assembly process does not require NIR activation; it occurs naturally when the distance between two micromotors is smaller than the capillary length. If the distance is too large, the micromotors are unable to assemble on their own. In such cases, NIR can be used to transport the micromotors closer together, facilitating the self-assembly process (Fig. S2a and Movie S5, ESI†). The assembly is reversible, as the micromotor doublets can be disassembled when the capillary attraction is disrupted. This can be achieved by depositing a low-surface-tension liquid onto the assembled structure. The low-surface-tension liquid, which is miscible with water, wets the micromotors, causing them to submerge underwater. As a result, the liquid menisci around the micromotors disappear, and the capillary attraction diminishes, causing the disassembly of the assembled structure through liquid flows induced by the

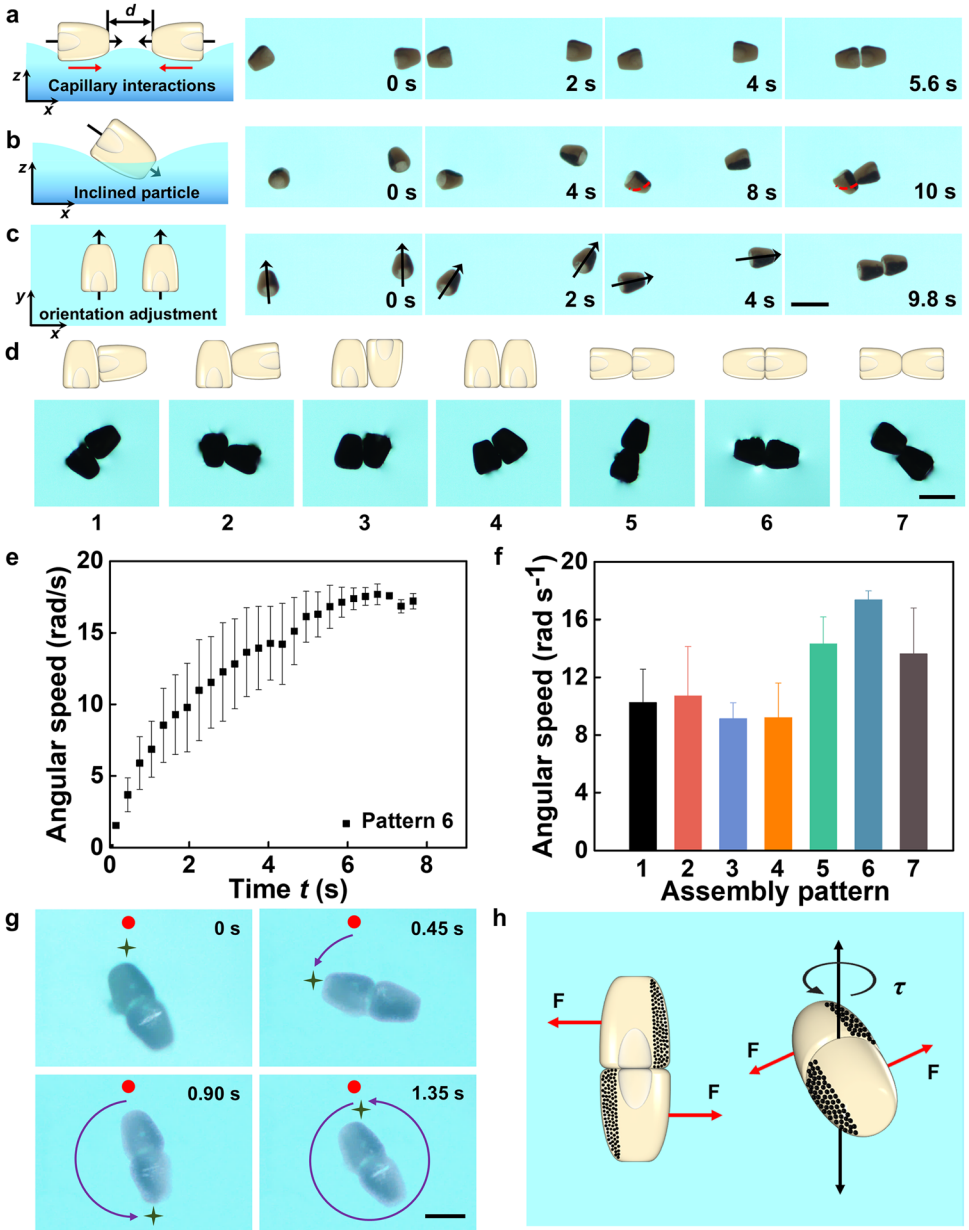

Fig. 3 Self-assembly. (a)–(c) Self-assembly *via* capillary interaction. The left side is schematic diagrams, and the right is the corresponding physical process, where the red dotted lines in (b) represent the contact line between water and the micromotor (images of 8 s and 10 s). (d) Double-motor self-assemblies. The upper and lower parts are schematic diagrams and actual pictures of seven patterns, respectively. (e) The relationship between angular speed and time (t) for pattern 6, which exhibits the highest ω_{max} (113 mW mm^{-2}). (f) Comparison of ω_{max} of the seven patterns. The three chain-like structures (patterns 5–7) possess relatively higher ω_{max} (113 mW mm^{-2}). (g) Temporal evolution of counterclockwise rotation of pattern 6. (h) Schematic diagram of the rotation of chain-like self-assemblies. Scale bars, 1 mm in (a)–(d) and 500 μm in (g).

coalescence of the droplet with the water surface. As shown in Fig. S2b and Movie S6 (ESI†), applying a droplet of low-surface-tension liquids, such as a 2% sodium dodecyl sulfate (SDS) solution or ethanol, onto the assembled structure results in disassembly, while high-surface-tension water cannot achieve this.

The shape anisotropy of the micromotors enhances the diversity of self-assembled patterns. Fig. 3(d) shows seven types of patterns formed by the self-assembly of two micromotors. We conducted 100 parallel experiments to determine the occurrence probability of each pattern, with results presented in Fig. S3a (ESI†). The chain-like structure is the most frequent, occurring nearly 60% of the time. We further explored the motion modes of these seven patterns under NIR irradiation at 113 mW mm^{-2} (Fig. S3b, ESI†). Remarkably, in addition to translation and revolution, a self-rotational motion emerges as the most probable. We investigated the rotational behavior of the seven patterns, as shown in Fig. 3(e) and Fig. S3c (ESI†). The angular speed initially increases with time until reaching a maximum value, indicating an equilibrium state of motion. Among these patterns, the three chain-like structures (patterns 5–7) exhibit higher angular speeds at equilibrium, with pattern 6

achieving the highest speed (17.4 rad s^{-1}, Fig. 3(f)). Fig. 3(g) and Fig. S3c (ESI†) illustrate the rotation of each structure (Movie S7), with the darker areas indicating the side with Fe_3O_4-NPs.

The motion modes of the three chain-like structures are highly predictable. When the Fe_3O_4-NPs are distributed on different sides of the two micromotors (a likely scenario during assembly), the two capillary forces generated under NIR irradiation create a torque (τ) that induces rotation (Fig. 3(g) and (h)). The rotation direction is determined by the polarity of the micromotors, as each micromotor moves from the hot, nanoparticle-rich side to the cooler, nanoparticle-free side (Fig. 3(g) and Fig. S3c, ESI†). In contrast, when the Fe_3O_4-NPs are located on the same side of both micromotors, the forces align in the same direction, resulting in translational motion (Fig. S3d, ESI†).

2.3 Multi-micromotor assembly

We now extend our analysis to multi-motor assemblies. The dual anisotropies in these micromotors result in an exponential increase in the number of possible patterns as the number of micromotors increases. For instance, while double-motor assemblies exhibit only three chain-like patterns, assemblies with three motors show a dramatic increase to sixteen chain-like patterns (Fig. 4 and Fig. S4a, ESI†).

We examined the motion characteristics of triple-motor assemblies under NIR irradiation at a power density of 58 mW mm^{-2}. Among the sixteen patterns, eight exhibit translational motion (Figs. S4a and b, ESI†). Four of these patterns have Fe_3O_4-NPs distributed on the same side (patterns 1–4 in Fig. S4a, ESI†). Interestingly, the other four patterns, with Fe_3O_4-NPs distributed on different sides (patterns 5–8 in Fig. S4a, ESI†), also demonstrate translational motion. In all eight patterns, the Fe_3O_4-NPs are located on the same side for the micromotors at the two edges of the chain-like structure, while the distribution of Fe_3O_4-NPs can be either on the same (patterns 1–4 in Fig. S4a, ESI†) or different (patterns 5–8 in Fig. S4a, ESI†) sides of the micromotor in the middle of the

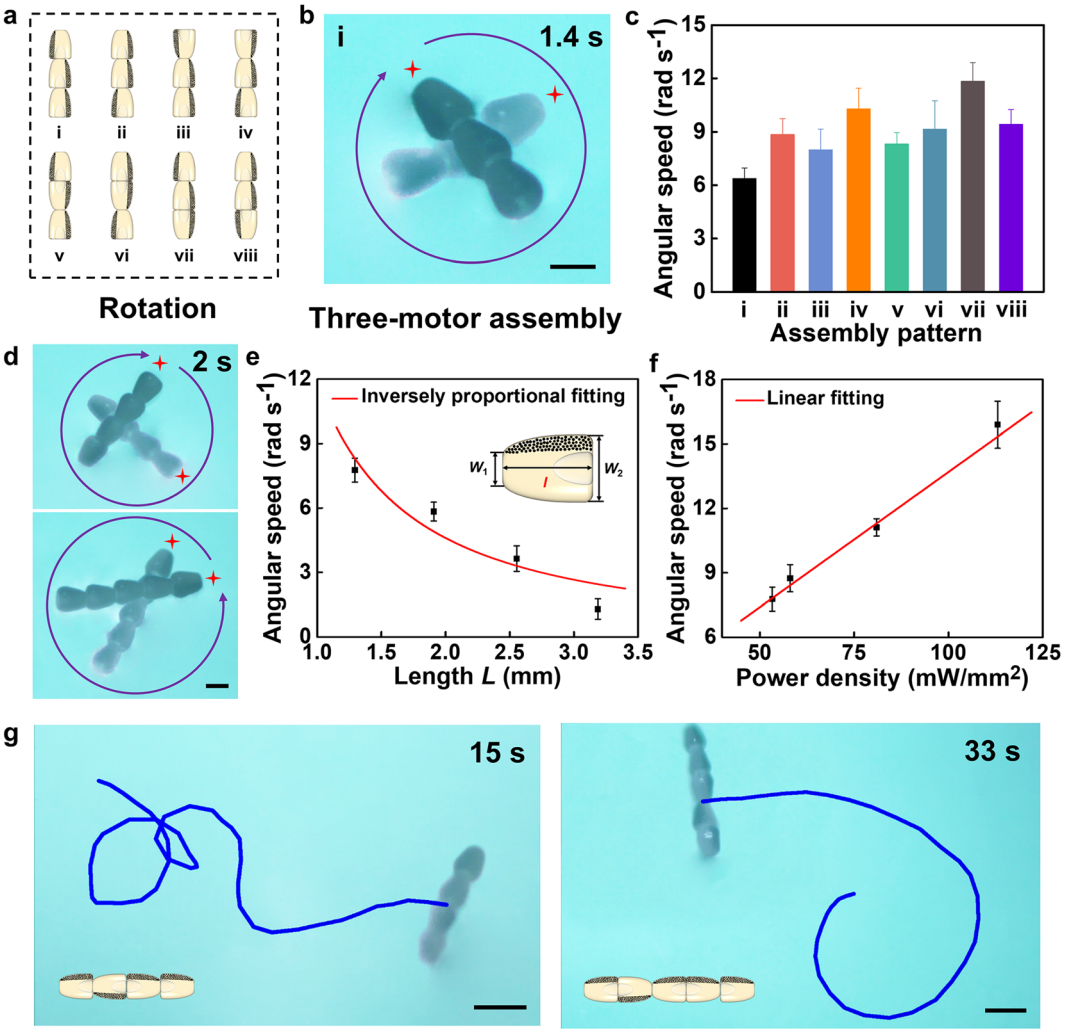

Fig. 4 Multi-motor assembly. (a) Patterns of triple-motor self-assembly exhibiting rotational motion. (b) Superimposed image of the rotation of pattern i. Scale bar, 500 μm. (c) Comparison of ω_{max} of the eight patterns. (d) The rotational motion of quadruple-motor (upper) and quintuple-motor (lower) self-assemblies. Scale bar, 500 μm. (e) The plot of ω_{max} *versus* L (53 mW mm^{-2}). The inset shows the dimensions of a single micromotor. (f) The relationship between ω_{max} and power density. (g) Combined motion modes of quadruple-motor (left) and quintuple-motor (right) self-assemblies. Scale bars, 1 mm.

assembled structure. This same-side distribution at the edges prevents torque generation, resulting in translational motion.

In contrast, the other eight patterns exhibit rotational motion, characterized by Fe_3O_4-NPs being distributed on different sides of the micromotors at the two edges (Fig. 4(a)), which is responsible for the torque generation. Fig. 4(b) and Fig. S4c (ESI†) show the rotation of the eight patterns in detail (Movie S8, ESI†). Similar to double-motor assemblies, the rotation direction of triple-motor assemblies is determined by the motion direction of the micromotors at the edges. A statistical analysis of the angular speeds of each pattern (Fig. 4(c)) reveals that pattern vii has the highest angular speed (11.8 rad s^{-1}).

For chain-like structures, the number of micromotors, or the chain length, significantly affects the motion speed of self-assembled structures. Therefore, it is crucial to understand the effect of chain length on angular velocity. We investigated the rotational characteristics of double-motor, triple-motor, quadruple-motor, and quintuple-motor assemblies with chain-like patterns under NIR irradiation at 53 mW mm^{-2}. Fig. 4(d) illustrates examples of rotational motion for quadruple-motor (upper image) and quintuple-motor (lower image) assemblies. As shown in Fig. 4(e), the maximum angular speed is inversely proportional to the chain length.

For micromotor assemblies, the propulsion force can be approximated as,

$$F_p \sim \Delta\gamma nl \sim \Delta\gamma L.$$

Here, $\Delta\gamma$ is the surface tension difference across the assembly, $L = nl$ is the total body length, n is the number of micromotors, and l is the length of each micromotor. The Reynolds number $\mathrm{Re} = \rho\nu L/\mu$ of the assembled structure is calculated to $\mathrm{Re} > 1$, where ρ is the density of water, ν is the motion velocity, and μ is the dynamic viscosity of water. The viscous drag force is assumed to be,

$$F_d \sim \rho{\nu_{max}}^2 C_d A \sim \rho(\omega_{max}L)^2 C_d n(W_1 + W_2)l \sim \rho C_d(W_1 + W_2){\omega_{max}}^2 L^3,$$

where C_d is the drag coefficient, A is the projected area of the assembly, v_{max} is the maximum motion velocity, ω_{max} is the maximum angular speed, and W_1 and W_2 are the widths of the smaller front and larger rear end, respectively (Fig. 4(e)). Assuming a balance between the propulsion and drag forces, $F_p \sim F_d$, at the maximum rotational velocity, ω_{max} can be estimated as,

$$\omega_{max} \sim \frac{1}{L}\sqrt{\frac{\Delta\gamma}{\rho C_d(W_1 + W_2)}}$$

indicating that ω_{max} is inversely proportional to L and decreases as the assembly size increases, consistent with the observation in Fig. 4(e). The influence of the micromotor's density is negligible, as its motion is confined to a plane parallel to the water surface and perpendicular to the gravitational direction. Given the low Reynolds number, viscous forces dominate over inertial forces, governing the motion at the low velocities in our experiments. The negligible role of inertia is further evidenced by the immediate cessation of the micromotor's movement when the NIR irradiation is switched off (Fig. 1(f)). However, the magnitude of inertial forces can still affect the drag coefficient (C_d), which in turn influences the angular velocity, as C_d is dependent on Re.

We also examined the relationship between angular speed and light intensity (113 mW mm^{-2}, 81 mW mm^{-2}, 58 mW mm^{-2}, 53 mW mm^{-2}), as shown in Fig. 4(f). The results indicate a linear increase in angular speed with increasing light intensity. Furthermore, the motion of quadruple-motor and quintuple-motor assemblies reveals a unique combined motion mode, consisting of translational and rotational motions (Fig. 4(g) and Movie S9, ESI†). This occurs when a micromotor near the edge has a different distribution of Fe_3O_4-NPs compared to the others, resulting in weak torque for rotational motion alongside the dominant translational motion due to the uniform Fe_3O_4-NP distribution in the majority of micromotors.

2.4 Superstructure assemblies

We investigated the superstructure assemblies comprising more than ten particles. As shown in Fig. 5(a), when the number of microparticles reaches ten (n = 10), the self-assembled structures roughly retain a single chain-like morphology. However, with twenty, thirty, forty, and fifty particles, the structures transition to fractal configurations composed of multiple-branched chains. Notably, parallel experiments (ten trials) revealed that patterns with the same number of microparticles exhibit similar characteristic radius r, defined as the radius of the smallest circle enclosing the pattern. Fig. 5(b) demonstrates that the characteristic radius scales with $\sim n^{2/3}$. Using the box-counting method, we measured the fractal dimension D_f of these fractal patterns (Fig. 5(c)), which is almost constant for all assembled structures with D_f = 1.5, independent of the number of microparticles.

For assemblies with small n, the distribution of Fe_3O_4-NPs is crucial in determining their motion behaviors (*e.g.*, $n \leq 5$), where the whole assembly is fully covered by the NIR laser spot. However, when the number of microparticles exceeds ten, the resulting superstructures have a size larger than that of the laser spot. In this scenario, not every microparticle is decisive in the motion. Instead, only localized microparticles exposed to the laser illumination can convert light into thermal energy for the motion (Fig. 5(d)). Therefore, the direction, trajectory, and even mode of motion can be tailored by exposing different parts of the superstructure to the NIR irradiation.

Additionally, we found that light and magnetic fields can guide microparticle self-assembling into predetermined patterns. As shown in Fig. 5(e) and Movie S10 (ESI†), by controlling microparticles to form various short chains of particular lengths, these chains can be positioned and combined under the guidance of the light or magnetic field to create complex patterns, such as English letters and Chinese characters. Using the same control methods, more intricate patterns were generated, including cartoon stick figures (Fig. 5(f)), the English word ''CITYU'', other Chinese characters, and the numbers ''2,'' ''3,'' and ''4'' under the influence of magnetic fields (Fig. S5, ESI†). This approach holds significant potential in

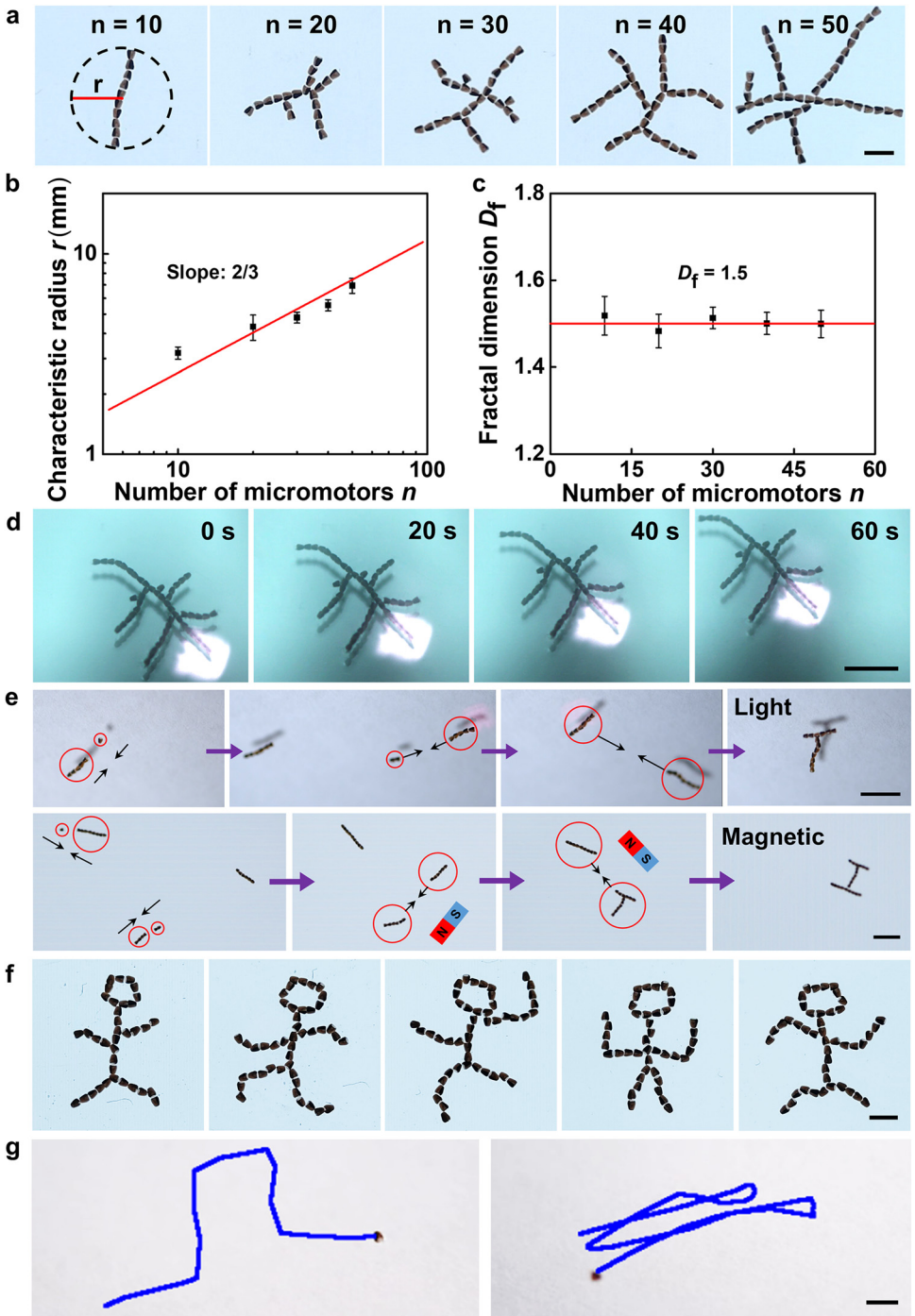

Fig. 5 Swarming of micromotor superstructures. (a) Examples of superstructures formed by ten, twenty, thirty, forty, and fifty micromotors. The characteristic radius of the pattern is represented by *r*. (b) Characteristic radius *versus* the number of micromotors (*n*). (c) The plot of fractal dimension D_f with *n*. (d) Movement of superstructures under NIR partial illumination. (e) The self-assembly process of micromotors regulated under light (upper row) and magnetic (lower row) fields, resulting in the formation of English letters and Chinese characters. (f) Cartoon stick figures formed through the magnetic field-assisted assembly. (g) Combing light and magnetic fields to drive the micromotor in complex motions, including detour and oscillatory trajectories. Scale bars, 2 mm in (a), (f), and (g), and 5 mm in (d) and (e).

constructing architectural intelligent materials and systems for information encoding.

The combination of light and magnetic fields enables more versatile and precisely controllable motion behaviors of micromotors. Light initiates the photothermal Marangoni effect to generate motion, while the magnetic field is used to adjust the micromotor's orientation, guiding its direction. This dual control allows for sophisticated motion capabilities, enabling arbitrary motion trajectories, as demonstrated by the detour and oscillatory motion behaviors (Fig. 5(g) and Movie S11,

ESI†). In these demonstrations, the light field drives the translational motion, while the magnetic field steers the micromotors during sudden turns.

3. Discussion

This study employs microfluidic technology to fabricate photothermal Marangoni micromotors, allowing precise control over their shape and material distribution, obviating the need for additional treatments such as functionalization. The micromotor is composed of PDMS microparticles integrated with Fe_3O_4-NPs, exhibiting dual anisotropy: shape anisotropy is characterized by a bullet-like shape with a smaller front and a larger rear end, while a unilateral distribution of Fe_3O_4-NPs marks material anisotropy. This configuration allows the micromotor to absorb NIR radiation and convert it into heat, thereby generating a surface tension gradient that propels the micromotor towards the non-Fe_3O_4 side. For an individual micromotor, a smaller lying angle θ tends to cause translational motion, while a larger θ tends to induce revolution motion, with the motion speed linearly increasing with light intensity.

Typically, achieving rotational motion requires complex structural design or fabrication processes, and once fabricated, the micromotor is limited to that specific motion mode. In contrast, this study demonstrates that simple self-assembly of micromotors can achieve rotational motion, with various self-assembled structures also enabling translational, revolution, and combined motions. The achievement of these functionalities circumvents the use of complex instruments, intricate design, and tedious processing steps, thereby endowing it with convenience and cost-efficiency. The self-assembly of micromotors is mediated by capillary interactions, with the most common configuration being a chain-like structure. By examining the motion of different self-assembled configurations, it is found that chain-like assemblies exhibit highly controllable and predictable motion behavior. The same-side distribution of Fe_3O_4-NPs produces translational motion, while hetero-lateral distribution can generate multiple motion modes. Compared to other photothermal micromotors, the micromotor developed in this work offers a simplified fabrication process and exhibits enhanced motion control under easily adjustable illumination strategies (Table S1, ESI†).[34,49–52]

Based on the aforementioned analysis, the motion of the micromotor assemblies is programmable. By customizing the pattern of the self-assembled structures, we can achieve the desired motion mode. This objective can be readily accomplished by manipulating the orientation, angle, and relative positioning of the micromotors on the water surface, as well as by varying the number of micromotors to modulate the motion speed. These outcomes are attained without necessitating elaborate post-processing or intricate structural designs but relying solely on the inherent self-assembly capabilities of the micromotors. Furthermore, the introduction of control fields, such as magnetic fields, can regulate the self-assembly process to form predetermined superstructures, potentially informing the fabrication of intelligent materials or structures.

4. Experimental details

4.1 Materials

The following materials were purchased and used upon received: PDMS (Sylgard 184, Dow Corning, 0.965 kg m^{-3}), sodium alginate (Aladdin), tetrasodium ethylenediaminetetraacetate dehydrate (EDTA-4Na, Macklin), calcium chloride ($CaCl_2$, Aladdin), poly(vinyl alcohol) (PVA, 87–89% hydrolyzed, Aladdin), distilled water (Watsons), silicone oil (viscosity of 1 mPa s, Aladdin), Fe_3O_4 nanoparticles (Zhong Hang Zhong Mai Materials, 5.18 kg m^{-3}), fluorescent particles (Bei Ting Measurement Technology), sodium dodecyl sulfate (SDS, Macklin), ethanol (Anaqua).

4.2 Experimental device

The microparticles employed in this study were fabricated using a co-flow microfluidic device. The device consisted of an inner cylindrical glass capillary with an inner diameter of 100 μm and an outer cylindrical glass capillary with an inner diameter of 900 μm. The outer capillary outlet was inserted into a Petri dish containing 10 wt% $CaCl_2$ solution, and both capillaries were connected to syringe pumps (Longer Pump, LSP01-1A) for liquid infusion.

4.3 Fabrication of anisotropic micromotors

The microparticle fabrication process contained three steps: microfiber production, droplet solidification, and microfiber dissolution. A mixture comprising PDMS (with 9 wt% curing agent), silicone oil, and Fe_3O_4-NPs was utilized as the inner phase liquid to generate PDMS microdroplets. The incorporation of silicone oil into the PDMS aimed to reduce the viscosity of the liquid, thereby facilitating droplet formation. The outer phase liquid was a 5 wt% NaAlg solution. A high-precision syringe pump (Longer Pump, LSP01-1A) delivered the liquids into the microfluidic device at controlled flow rates, resulting in the shearing of the inner phase liquid to form a droplet array. Upon the NaAlg solution exiting the capillary into the Petri dish, ion crosslinking solidified the NaAlg with $CaCl_2$, forming hydrogel microfibers encapsulating PDMS microdroplets. These hydrogel microfibers were subsequently dried to solidify the PDMS droplets. The curing environment determined the spatial distribution of the Fe_3O_4-NPs in PDMS microparticles: room temperature curing localized nanoparticles on one side while curing at 80 °C for 30 minutes achieved uniform distribution. A 2 wt% EDTA-4Na solution dissolved the alginate microfibers, releasing the cured PDMS microparticles. These microparticles were then washed, dried, collected, and stored.

4.4 Movement and characteristics of micromotors

An 808 nm NIR laser (1200 mW, FUZHE) was used as the light source. The motion of the micromotors was captured using a high-speed camera (Fastcam Mini, Photron) at frame rates up to 100 frames per second (fps). The micromotors were characterized *via* an inverted microscope (Nikon ECLIPSE Ts2) and scanning electron microscope (JEOL JSM 5600). The dynamic properties of the micromotors were analyzed using ImageJ software (National Institutes of Health).

Author contributions

P. Z. conceived the research. P. Z. and W. Z. designed the experiments. W. Z. performed the experiments. S. W., Y. Z., Y. L., S. T., and Y. Z. assisted W. Z. in experiments. P. Z. and W. Z. performed the theoretical analysis, analyzed the data, and wrote the manuscript. P. Z. supervised the research. All authors commented on the paper.

Data availability

The data supporting this article have been included as part of the ESI† and are available from the corresponding authors.

Conflicts of interest

There are no conflicts to declare.

Acknowledgements

The financial support from National Natural Science Foundation of China (52303046), the Research Grants Council of Hong Kong (21213621), Shenzhen Science and Technology Program (JCYJ20220530140812028), and the City University of Hong Kong (7005936 and 7006097) is gratefully acknowledged.

References

1 J. H. Zhang, A. Laskar, J. Q. Song, O. E. Shklyaev, F. Z. Mou, J. G. Guan, A. C. Balazs and A. Sen, *ACS Nano*, 2023, **17**, 251–262.
2 Y. X. Gao, L. Y. Ou, K. F. Liu, Y. Guo, W. Y. Li, Z. Xiong, C. J. Wu, J. H. Wang, J. Y. Tang and D. Li, *Angew. Chem., Int. Ed.*, 2024, **63**, e202405895.
3 A. Pena-Francesch, J. Giltinan and M. Sitti, *Nat. Commun.*, 2019, **10**, 3188.
4 A. Q. Chen, X. H. Ge, J. Chen, L. Y. Zhang and J. H. Xu, *Lab Chip*, 2017, **17**, 4220–4224.
5 L. J. Cai, D. Y. Xu, Z. Y. Zhang, N. Li and Y. J. Zhao, *Research*, 2023, **6**, 0044.
6 J. X. Li, B. Esteban-Fernandez de Ávila, W. Gao, L. F. Zhang and J. Wang, *Sci. Robot.*, 2017, **2**, eaam6431.
7 L. J. Cai, C. Zhao, H. X. Chen, L. Fan, Y. J. Zhao, X. Y. Qian and R. J. Chai, *Adv. Sci.*, 2022, **9**, 2103384.
8 Y. Dong, L. Wang, Z. F. Zhang, F. T. Ji, T. K. F. Chan, H. J. Yang, C. P. L. Chan, Z. X. Yang, Z. G. Chen, W. T. Chang, J. Y. K. Chan, J. J. Y. Sung and L. Zhang, *Sci. Adv.*, 2022, **8**, eabq8573.
9 W. Q. Hu, G. Z. Lum, M. Mastrangeli and M. Sitti, *Nature*, 2018, **554**, 81–85.
10 H. J. Zhou, C. C. Mayorga-Martinez, S. Pané, L. Zhang and M. Pumera, *Chem. Rev.*, 2021, **121**, 4999–5041.
11 G. Loget and A. Kuhn, *Nat. Commun.*, 2011, **2**, 535.
12 S. T. Chang, V. N. Paunov, D. N. Petsev and O. D. Velev, *Nat. Mater.*, 2007, **6**, 235–240.
13 W. W. Qin, T. H. Peng, Y. J. Gao, F. Wang, X. C. Hu, K. Wang, J. Y. Shi, D. Li, J. C. Ren and C. H. Fan, *Angew. Chem., Int. Ed.*, 2017, **129**, 530–533.
14 A. M. Brooks, M. Tasinkevych, S. Sabrina, D. Velegol, A. Sen and K. J. M. Bishop, *Nat. Commun.*, 2019, **10**, 495.
15 H. R. Ding, P. S. Kollipara, Y. Kim, A. Kotnala, J. G. Li, Z. H. Chen and Y. B. Zheng, *Sci. Adv.*, 2022, **8**, eabn8498.
16 L. L. Xu, F. Z. Mou, H. T. Gong, M. Luo and J. G. Guan, *Chem. Soc. Rev.*, 2017, **46**, 6905–6926.
17 F. Nan, X. Li, S. L. Zhang, N. Jack and Z. J. Yan, *Sci. Adv.*, 2022, **8**, eadd6664.
18 D. Okawa, S. Pastine, A. Zettl and J. Fréchet, *J. Am. Chem. Soc.*, 2009, **131**, 5396–5398.
19 C. Maggi, F. Saglimbeni, M. Dipalo, F. A. De and R. L. Di, *Nat. Commun.*, 2015, **6**, 7855.
20 Y. Choi, C. Park, A. C. Lee, J. Bae, H. Kim, H. Choi, S. W. Song, Y. Jeong, J. Choi, H. Lee, S. Kwon and W. Park, *Nat. Commun.*, 2021, **12**, 4724.
21 X. X. Ke, H. C. Yong, F. K. Xu, H. Ding and Z. G. Wu, *Nat. Commun.*, 2024, **15**, 1491.
22 K. L. Zhang, Y. K. Ren, M. Y. Zhao, T. Y. Jiang, L. K. Hou and H. Y. Jiang, *Anal. Chem.*, 2021, **93**, 2560–2569.
23 V. Frumkin, K. Gommed and M. Bercovici, *Phys. Rev. Fluids*, 2019, **4**, 074002.
24 É. O'Neel Judy, D. Nicholls, J. Castañeda and J. G. Gibbs, *Small*, 2018, **14**, 1801860.
25 K. Hou, D. S. Guan, H. Y. Li, Y. Q. Sun, Y. Long and K. Song, *Sci. Adv.*, 2021, **7**, eabh3051.
26 S. Palagi, A. G. Mark, S. Y. Reigh, K. Melde, T. Qiu, H. Zeng, C. Parmeggiani, D. Martella, A. Sanchez-Castillo, N. Kapernaum, F. Giesselmann, D. S. Wiersma, E. Lauga and P. Fischer, *Nat. Mater.*, 2016, **15**, 647–653.
27 X. Zhou, Z. T. Li, L. H. Tan, Y. Zhang and Y. P. Jiao, *ACS Appl. Mater. Interfaces*, 2020, **12**, 23134–23144.
28 J. B. Huang, X. Y. Yu, L. Y. Li, W. X. Wang, H. T. Zhang, Y. Zhang, J. Zhu and J. Ma, *ACS Nano*, 2024, **18**, 2006–2016.
29 J. T. Tong, D. L. Wang, Y. Liu, X. Lou, J. W. Jiang, B. Dong, R. F. Dong and M. C. Yang, *Proc. Natl. Acad. Sci. U. S. A.*, 2021, **118**, e2104481118.
30 X. D. Wang, L. G. Dai, N. D. Jiao, S. Tung and L. Q. Liu, *Chem. Eng. J.*, 2021, **422**, 129394.
31 C. L. Huang, J. A. Lv, X. J. Tian, Y. C. Wang, Y. L. Yu and J. Liu, *Sci. Rep.*, 2015, **5**, 17414.
32 D. M. Li, F. Y. Guo, Z. M. Cui, J. Zhou, Y. Z. Zhai, Y. J. Du, J. C. Liu, N. Wang and Y. Zhao, *ACS Appl. Mater. Interfaces*, 2020, **12**, 53503–53509.
33 M. Ibele, T. Mallouk and A. Sen, *Angew. Chem., Int. Ed.*, 2009, **48**, 3308–3312.
34 Z. Y. Deng, F. Z. Mou, S. W. Tang, L. L. Xu, M. Luo and J. G. Guan, *Appl. Mater. Today*, 2018, **13**, 45–53.
35 D. Singh, U. Choudhury, P. Fischer and A. Mark, *Adv. Mater.*, 2017, **29**, 1701328.
36 G. Whitesides and B. Grzybowski, *Science*, 2002, **295**, 2418–2421.
37 Z. H. Lin, C. Y. Gao, M. L. Chen, X. K. Lin and Q. He, *Curr. Opin. Colloid Interface Sci.*, 2018, **35**, 51–58.

38 H. R. Jiang, N. Yoshinaga and M. Sano, *Phys. Rev. Lett.*, 2010, **105**, 268302.
39 Q. L. Zhang, R. F. Dong, X. Y. Chang, B. Y. Ren and Z. Tong, *ACS Appl. Mater. Interfaces*, 2015, **7**, 24585–24591.
40 J. E. Park, S. J. Park, A. Urbas, Z. Ku and J. J. Wie, *ACS Nano*, 2022, **16**, 3152–3162.
41 C. M. Zhou, P. A. Zhu, Y. Tian, M. Xu and L. Q. Wang, *ACS Nano*, 2019, **13**, 6319–6329.
42 Z. C. Ma, J. H. Fan, H. S. Wang, W. D. Chen, G. Z. Yang and B. Han, *Small*, 2023, **19**, 2300469.
43 P. A. Zhu and L. Q. Wang, *Chem. Rev.*, 2022, **122**, 7010–7060.
44 S. Y. Wang, S. C. Li, W. C. Zhao, Y. Zhou, L. Q. Wang, J. Aizenberg and P. A. Zhu, *Lab Chip*, 2024, **24**, 4073–4084.
45 Y. H. Lu, S. H. Wang and P. A. Zhu, *Ind. Chem. Mater.*, 2024, **2**, 441–450.
46 P. A. Zhu, R. F. Chen, C. M. Zhou, M. Aizenberg, J. Aizenberg and L. Q. Wang, *Adv. Mater.*, 2021, **33**, 2008558.
47 G. J. Gittens, *J. Colloid Interface Sci.*, 1969, **30**, 406–412.
48 R. Ismagilov, A. Ismagilov, N. Bowden and G. Whitesides, *Angew. Chem., Int. Ed.*, 2002, **41**, 652–654.
49 W. Wang, Y. Q. Liu, Y. Liu, B. Han, H. Wang, D. D. Han, J. N. Wang, Y. L. Zhang and H. B. Sun, *Adv. Funct. Mater.*, 2017, **27**, 1702946.
50 M. J. Xuan, R. Mestre, C. Y. Gao, C. Zhou, Q. He and S. Sánchez, *Angew. Chem., Int. Ed.*, 2018, **57**, 6838–6842.
51 Z. G. Wu, X. K. Lin, Y. Wu, T. Y. Si, J. M. Sun and Q. He, *ACS Nano*, 2014, **8**, 6097–6105.
52 W. T. Cao, W. Feng, Y. Y. Jiang, C. Ma, Z. F. Zhou, M. G. Ma, Y. Chen and F. Chen, *Mater. Horiz.*, 2019, **6** 1057–1065.

